Monitoring the TROPOMI-SWIR module instrument stability using desert sites

Tim A. van Kempen[1], Filippo Oggionni[2], and Richard M. van Hees[1]

[1]SRON Netherlands Institute for Space Research, Sorbonnelaan 2, 3584 CA, Utrecht, the Netherlands
[2]Delft University of Technology, Faculty of Aerospace Engineering, Kluyverweg 1, 2629 HS, Delft, the Netherlands

Correspondence: Tim van Kempen (t.a.van.kempen@sron.nl)

Abstract. Since its launch in 2017, the TROPOMI instrument on S-5P has provided very high quality data using daily global coverage for a number of key atmospheric trace gasses. Over its first 1,000 days in operations, the SWIR module has been very stable and the continuously monitored calibration has remained of high quality. This calibration relies on a combination of extensive pre-launch and post-launch measurements, complemented by regular monitoring of internal light sources and background measurements. In this paper we present a method and results for independent validation of the SWIR module calibration and instrument stability by examining the signal stability of a sample of 23 pseudo-invariant calibration desert sites. The data covers over two years of operational data. With a Lambertian surface assumption, the results show that the SWIR module has little to no instrument degradation down to an accuracy of about 0.3% per year, validating results obtained from the internal calibration suite. The method presented here will be used as ongoing validation of the SWIR calibration.

1 Introduction

The Tropospheric Monitoring Instrument (TROPOMI[1]) is the sole instrument on the Sentinal-5 Precursor mission (better known as S-5P Veefkind et al., 2012). S5-P is part of the ESA Copernicus program and is the first mission covering the atmospheric composition. Its aim is to quantify specific trace-gas column densities. With the very wide swath opening of more than 60 degrees, TROPOMI can provide daily global coverage. The four channels (UV, UVIS, NIR and SWIR) give unprecedent view of atmospheric composition and evolution on timescales of days to years. Launched in late 2017, TROPOMI started regular operations in April 2018 after in-flight commissioning and science verification. The instrument has been shown to be very stable with only limited degradation (van Kempen et al., 2019; Ludewig et al., 2020). The SWIR module covers a wavelength range between 2300 and 2380 nm and has been designed for the carbon-monoxide (CO) and methane (CH_4) products, (e.g. Hu et al., 2018; Borsdorff et al., 2018; Pandey et al., 2019; Zhang et al., 2020).

Since the start of nominal operations, TROPOMI has been in excellent health and the calibration has remained stable, in particular the SWIR module (van Kempen et al., 2019; Ludewig et al., 2020). For its calibration, TROPOMI relies on the

---

[1]TROPOMI is a collaboration between Airbus Defence and Space Netherlands, KNMI, SRON and TNO, on behalf of NSO and ESA. Airbus Defence and Space Netherlands is the main contractor for the design, building and testing of the instrument. KNMI and SRON are the principal investigator institutes for the instrument. TROPOMI is funded by the following ministries of the Dutch government: the Ministry of Economic Affairs, the Ministry of Education, Culture and Science, and the Ministry of Infrastructure and the Environment.

results from the on-ground campaign (Kleipool et al., 2018; Tol et al., 2018; van Hees et al., 2018), regular solar irradiance measurements and background measurements, as well as measurements using on-board lights that are part of the integrated calibration unit (ICU) (see van Kempen et al., 2019, for an overview of on-board lights relevant to the SWIR module). The on-board lights consist of a White Light Source (WLS), Dedicated LED (DLED), five diode lasers and a common Led (CLED).The on-board lights have various goals to maintain specific parts of the calibration; e.g. the diode lasers are aimed at characterizing any ISRF (Instrument Spectral Response Function) and/or straylight changes (Tol et al., 2018; van Hees et al., 2018). In-flight, the main goal is the relative calibration, although some parts of the absolute calibration can be derived. The results reveal instrument instabilities for the SWIR module to be less than 0.5% over the first year. This stability has been improved by regular monitoring (see e.g. mps.tropomi.edu), with the SWIR module stable down to 0.3% or less over the first two or three years of regular operations.

TROPOMI products are provided either as L1b products, which consists of calibrated radiance and irradiance data, or L2 products, which consist of the retrieved column densities of selected gas tracers. Data quality from TROPOMI is validated using a range of space-based, airborne and ground-based networks and/or dedicated measurements[2]. These validations are done using the full range of the L2 products. However, these efforts, which are part of the Mission Performance Center of S-5P do not include independent validation of the L1b data quality due to the complexity of the task. Various scenarios have been discussed, but in essence, L1b validation is much more complicated and cannot easily be carried out using automated ground-stations.

Nevertheless, validation of the L1b product serves two important goals. First, it provides validation of the quality of the absolute and relative radiometric calibration and thus the quality of the calibration key data in use. Second, it provides an independent quantification of the instrument stability. The first goal requires independent ground-based measurements. These typically originate from co-incidental space-based measurements (so-called cross-calibration, see e.g. Chander et al., 2013; Kataoka et al., 2017) or from complementary ground measurements through Vicarious Calibration (e.g. Kuze et al., 2014; Bruegge et al., 2019b, a). Both have strict limitations due to instrument properties, temporal difference or spatial coverage. However, validation of instrument stability has less stringent demands and can be carried out by monitoring Pseudo-Invariant Calibration Sites, from hereon referred to as PICS. PICS are locations on Earth that are typically free of precipitation, vegetation and/or clouds. They are relatively free of annual changes (e.g. due to vegetation) and posses a homogeneous surface. Desert locations are typically well suited as PICS. PICS have been in use as calibration sites since the mid-90s (Cosnefroy et al., 1996; Lacherade et al., 2013; Bacour et al., 2019), but are almost exclusively used by CCD camera's in the visible part of the spectrum. Other well-known sites include RailRoad Valley Playa (Nevada, US), Gobabeb (Namibia) or Boatou (China), all part of the RADCAL network (Bouvet et al., 2019).

Note that even in optimal circumstances, annual variations may exist, due to e.g. moisture content or small vegetation, both in the top soil. Non-lambertian reflectance components of the surface is expressed through the Bidirection Reflectance Distribution Function (BRDF) which determines into which directions sunlight is reflected.

---

[2]Please see VDAF facility at http://mpc-vdaf.tropomi.eu for up to date validation activities.

55 The BRDF of desert sand, in particular its accuracy and effect at off-nadir viewing angles, has been described and characterized by Bruegge et al. (2019a). They find that desert sand has a characteristic 'hot-spot' in the backwards direction of the incoming solar radiation. They also show that these BRDFs are not well characterized at large off-nadir viewing angles, with differences of 5% in a normalized solution w.r.t. the zenith shown as typical. The MODIS BRDF product (Schaaf et al., 2011) provides world-wide coverage with a 16-day interval but also suffers from inaccuracies as described in Bruegge et al. (2019a)

60 due to saturation of the detector. These are relevant for TROPOMI, due to its very wide swath.

In this paper we present an analysis of the site stability of a sample of 23 PICS in the Saharan, Arabian and Namibian deserts[3]. The sample was adopted from the analysis of Bacour et al. (2019), which itself revisited the original Saharan PICS sample from Cosnefroy et al. (1996) and Lacherade et al. (2013). Most analyses of PICS sites are done at visible wavelengths and/or at high resolutions of imagers. In this analysis, we will use continuum channels of the TROPOMI SWIR channel

65 assuming a Lambertian surface. In addition, no atmospheric correction will be applied. Section 2 provides the final sample, while the data usage of TROPOMI is presented in Section 3. This includes data filters and restrictions as well as the assumptions in our analysis. Section 4 gives the results while the impact is discussed in Section 5.

2 Saharan sites

Saharan PICS have been used for monitoring for a large number of sensors (e.g. Cosnefroy et al., 1996; Lacherade et al., 2013;

70 Bacour et al., 2019). These studies have shown the Sahara to be reasonably stable across large spatial scales and relatively invariant in time. The most recent in-depth review of the spatial and temporal variability of Saharan PICS can be found in Bacour et al. (2019) where the original lists of Cosnefroy et al. (1996); Lacherade et al. (2013) were inspected. An update of coordinates was given as compared to the original locations of Cosnefroy et al. (1996), as well as a quantified ordering on spatial homogeneity across 20 and 100 kilometers as well as temporal stability. In this study we have adopted the final sample

75 of Bacour et al. (2019) in their Tables 2 and 3. We will be using their coordinates to track the temporal variability of the SWIR channel continuum signal. As a typical TROPOMI pixel is at least 7x5 km^2 but can be as large as 20x7 km^2 (especially during the early parts of operations), the sites are inspected on their temporal stability and spatial homogeneity at 20 km (TVar (20km) and SHom(20km), as reported in Table 2 of Bacour et al. (2019).

3 TROPOMI Data

80 S5-P has daily overpasses over all sites shown in Table 1. For most sites, multiple overpasses only exist every ∼5 days due to the proximity to the equator. An overpass is valid if a pixel is located less than 0.2 degrees from the reference location given in Table 1. At the equator this equals 22 km. At typical Saharan latitudes, the separation is less then 20 km. Note that if multiple pixels qualify, only the pixel with the smallest separation to the reference position is used. TROPOMI data was processed using the operational version of the L1b version 01.00.00. Several filters are applied to improve the overall data quality. These are

---

[3]For simplicity, we will refer to this sample as the Saharan PICS sample, even though not all sites are located in the Saharan region

Table 1. Alphabetical list of Saharan PICS from Bacour et al. (2019) with latitude longitude following updated coördinates. Time variability and spatial homogeneity are given for reference.

Site	Latitude degree	Longitude degree	Tvar %	Svar %
Algeria1	23.83	-0.76	2.1	0.3
Algeria2	25.66	-0.62	2.0	0.7
Algeria3	30.63	7.83	2.0	0.7
Algeria4	29.99	5.10	1.8	0.5
Algeria5	31.16	2.24	2.1	0.8
AlgeriaPICSAND1	31.70	8.35	2.1	0.6
Arabia1	19.80	47.07	1.4	0.4
Arabia2	20.19	51.63	1.4	0.2
Arabia3	28.80	43.05	2.1	0.7
ArabiaPICSAND1	29.26	40.91	1.9	0.5
Egypt1	26.61	26.22	1.9	0.5
Libya1	24.65	13.25	2.1	0.6
Libya2	25.08	20.77	2.0	0.4
Libya3	23.22	23.23	1.4	0.4
Libya4	28.67	23.42	2.1	0.6
Mali1	19.14	-5.77	2.2	0.3
Mauritania1	19.51	-8.57	1.9	0.6
Mauritania2	19.78	-8.89	1.9	0.6
NamibiaPICSAND1	-25.00	15.25	1.2	0.9
Niger1	20.26	9.64	2.1	0.3
Niger2	21.33	10.60	2.2	0.6
Niger3	21.51	7.86	2.3	1.2
Sudan1	22.11	28.11	1.5	0.5
SudanPICSAND1	17.26	25.53	1.7	0.7
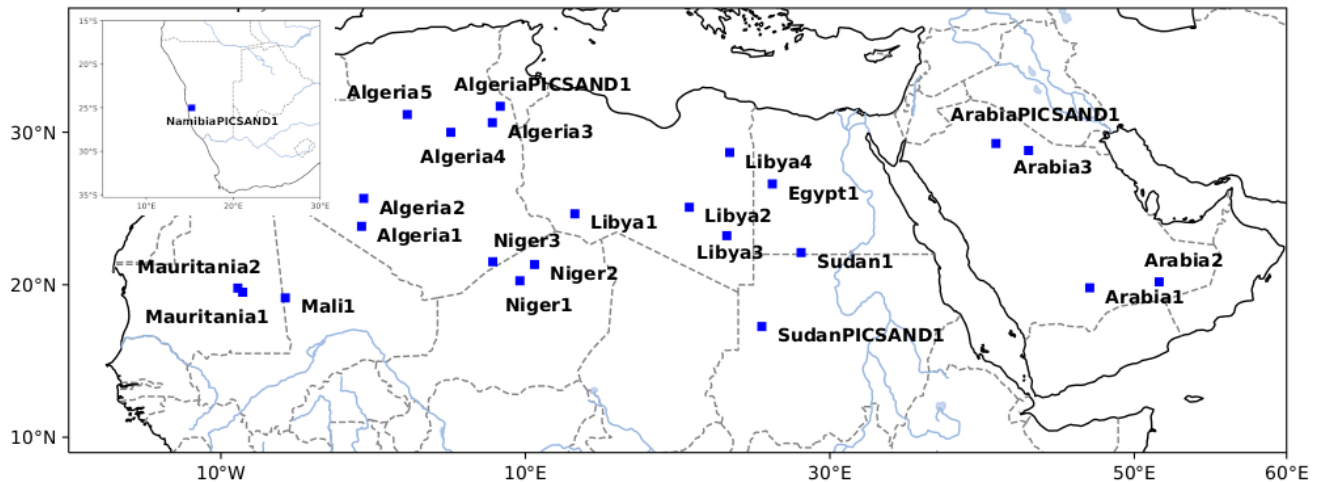
Figure 1. Location of Saharan and Arabian PICS. The PICS in the Namibian desert is shown as an inset.

listed in Table 2. Apart from the separation restriction, the viewing zenith angle must be smaller than 50 degrees, the cloud fraction of the pixel must be below 0.02, a successful and valid irradiance measurement should have been taken within a day of the overpass and the solar zenith angle must be below 60 degrees[4]. With the constraints described above, the largest variable parameter is the size of the TROPOMI overpass pixel. The size of a TROPOMI pixel is dependent on its location in the swath. At nadir, a typical TROPOMI pixel at SWIR wavelength is 7×7 km^2, while at the edge pixels can dramatically increase in size in the across-track direction, growing to sizes of up to 7×26 km^2. Note that after August 2019, this was reduced to 5.5×7 km^2 due to shorter integration times. As seen from Bacour et al. (2019), spatial homogeneity at larger scales (i.e. 100 km) can be significantly worse than its counterpart at 20 km scales. As such, it is imperative to avoid 'contamination' from large scales and focus only on the central regions. TROPOMI-SWIR soundings are thus restricted to viewing zenith angles of 50 degrees or less. Effects of larger viewing angles will be investigated in a future paper. Effectively this constrains soundings to positions away from the edges of the swath. This also automatically limits the pixel to a maximum pixel size in the across-track direction, while in the along-track dimension the resolution is set by the sampling time. The pixel size is thus dependent on the location through the viewing angle and on the date due to the change in integration time. In general, pixels are always smaller than 7 km in the along-track and 8.5 km in the across-track.

A choice was made to include relatively large viewing angles (up to 50 degrees) but exclude more extreme angles (TROPOMI can observe at almost 65 degrees). The alternatives, either limits to small viewing zenith angles or including all viewing angles, either severely constrained the available data or introduced additional scatter. Other alternatives, such as binning the data and removing angle-dependencies in the scatter did not improve the data. To compare data over the full time-span, data is corrected

---

[4]Note that this is a general restriction. Due to the early afternoon overpass time of S-5p, all measurements pass this restriction. It is included for completeness in the methodology.

Table 2. Constraints used for monitoring of the TROPOMI-SWIR radiance.

Constraints	
Overpass separation	<0.2 degree
Instrument Zenith Angle	<50 degree
Cloud Fraction	<0.02
Irradiance separation	<1 day
Solar Zenith Angle	<60 degree
Continuum wavelengths	[2312.7,2312.9] nm

by dividing by the cosine of the solar zenith angle. An additional constraint to limit the maximum solar zenith angle was implemented to filter a few problematic cases during winter times.

105 Cloud fraction is defined as a number between 0 and 1 representing the area of a pixel covered by clouds. A number of 0 is completely cloud-free, while 1 represents a pixel completely covered by clouds. The cloud fraction information was extracted from the support data included in the operational data product of the CH_4 $'offline'$ processor, version 1.2.0. Given the straylight correction as defined in Tol et al. (2018) and applied in the processor, no filtering was used for cloud presence beyond the sounding pixel.

110 Last but not least, soundings are required to have a valid irradiance measurement using TROPOMI-SWIR within a day. This filter is aimed at possible problematic soundings taken after an orbit maneuver or anomaly. This affects less than 0.1% of all TROPOMI measurements.

If an overpass is considered valid, the radiance is derived by taking the median signal for all pixels with center calibrated wavelength between 2312.7 to 2312.9 nanometers. Deep absorption features of CH_4 as well as H_2O are avoided. Uncertainty

115 of the radiance measurements is propagated at each correction using gaussian error propagation. Note that the uncertainty on the radiance of a sounding is small and includes only the shot noise of the detector, photon noise and uncertainties of the calibration data included during L1b processing.

3.1 Lambertian surface and atmospheric correction assumptions

For our analysis, the surface is assumed to be Lambertian in nature. It is well documented that off-nadir soundings are affected

120 by non-Lambertian effects (e.g. Bruegge et al., 2019a). Although correction routines can be applied, these often rely on ground measurements to derive the BRDF correction factors within a modified Rahman-Pinty-Verstraete (mRPV) model (Rahman et al., 1993b, a). Even in such a well-characterized site such as the Railroad valley playa, differences larger than 5% are seen in normalization factor (Bruegge et al., 2019b, a). These differences appear to be dependent on measurements used to derive the free parameters in a mRPV model. Ground measurements are not available for any of the sites listed in Table 1. Measurements

125 from space, such as MODIS or MISR, are typically of insufficient quality to reliably improve the data due to saturation effects and/or lack of wavelength coverage (Schaaf et al., 2011; Bruegge et al., 2019a). This is particularly apparent at larger viewing

zenith angles. Various studies Bruegge et al. (2019b, a); Kuze et al. (2014)indicate that this assumption will cause the largest scatter. In theory, the very large swath of TROPOMI is well-suited to characterize this effect in more detail, following e.g. the results as presented in Bruegge et al. (2019b, a). However, this effect is considered to be beyond the scope of this work; exploration of BRDF effects can only be carried out at instrumented sites such as Railroad Valley due to the need for validation.

Similarly, the lack of atmospheric correction applied to the data also may introduce additional scatter and or effects. The most important effect is due to varying aerosol densities. This effect is assumed to be relatively small at 2.3 micron wavelengths. Analysis did reveal that these assumptions are the most likely origin for a secondary yearly variation introduced due to the dependency of solar angles to the date. This is revealed as a sine wave with a 365-day period. This sine wave is fitted and removed from the data. The effects are discussed in section 4.2. Future work (van Kempen et al., in prep) will explore non-Lambertian and atmospheric correction effects for TROPOMI SWIR wavelengths.

3.2 TROPOMI data quality

The TROPOMI-SWIR response has been shown to be extremely stable over the first year (van Kempen et al., 2019) with no detector degradation seen. This has been corroborated by the ongoing monitoring of the calibration carried out at SRON and KNMI[5] Degradation of the transmission is below 0.2% for the detector median. Regions of the detector also do not show degradation below the accuracy limits of the stability of the white light source. or the dedicated LED. This allows two key assumptions to be made for this work. First, change in signal above 2% is difficult to attribute to the instrument. Second, any degradation seen in the signal above the desert Sahara will be representative over a large part of the columns[6] associated with 2312.7 to 2312.9 nm, only excluding the top and bottom parts of the detector which correspond to viewing angles larger than 50 degrees. Solar calibration over this region shows deviations less than 0.2% over the time period presented in this paper.

4 Results

Table 3 shows the median radiance and its standard deviation (both in absolute and relative scales) of accepted soundings for all sites from a period starting April 28th 2018 to 1st October 2020. In addition to these statistical properties, the slope of a linear fit over 1,000 days is given. This linear fit can be used as a quantification of potential degradation. This can be compared to the SWIR stability as seen in van Kempen et al. (2019); Ludewig et al. (2020). E.g., this stability should be similar to the trends seen in the DLED, WLS and transmission, as shown in Figures 23, 24 and 25 of van Kempen et al. (2019). Note that the DLED has its own degradation. Figure 2 shows the complete time series of four sites of our sample. These four sites were chosen at random to represent the sample. The results of all other sites are presented in given in supplemental material. Figure 3 gives two examples of the sine wave that was fitted and subsequently corrected for.

Figure 4 shows the distribution of standard deviations and slopes of the linear fits of the full sample.

---

[5]See https://www.sron.nl/tropomi-swir-monitoring/ and http://mps.tropomi.eu/dashboard for daily updates and weekly and monthly reports.

[6]In following with agreed TROPOMI convention, the directions on the SWIR detector are defined as the spectral axis being the x-axis and the spatial (i.e. swath) direction being the y-axis.
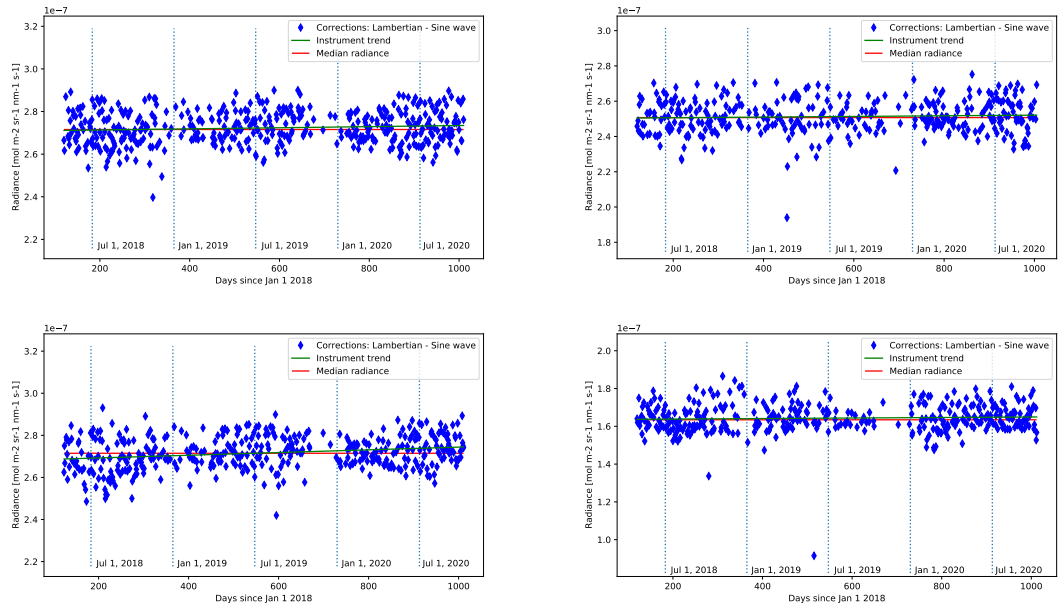
Figure 2. Continuum radiance of Egypt1 (top left), Algeria3 (top right), Libya3 (bottom left) and NamibiaPICSAND1 (bottom right) using a zenith angle filter of 50 degrees. Shown are all soundings over a period of more than 1,000 days, starting 28th of April 2018. The median radiance (red) and a linear fit (green) are shown with lines. Data has been corrected for the solar zenith angle at each individual overpass and assuming the surface is Lambertian. A yearly variation has been corrected using a fitted sine wave with a period of 365 days.
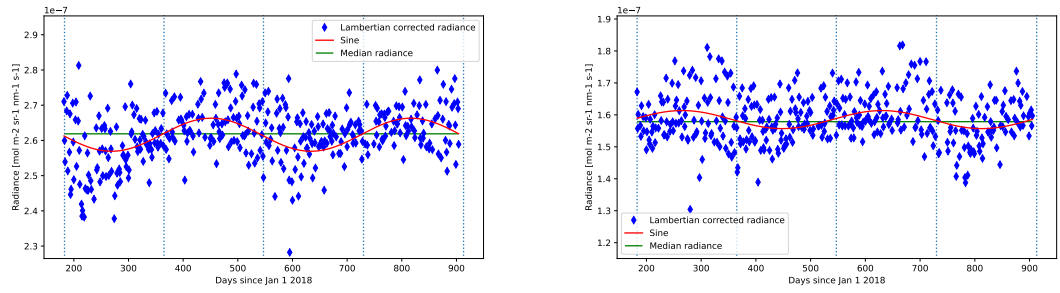
Figure 3. Continuum radiance of Libya3 (left) and NamibiaPICSAND1 (right) using a zenith angle filter of 50 degrees without the yearly sine variation removed. Shown are all soundings over a period of more than 1,000 days, starting 28th of April 2018. The median radiance (green) and a fitted sine (red) are shown. Data has been corrected for the solar zenith angle at each individual overpass and assuming the surface is Lambertian. Data of late 2019 is included to better illustrate fit. During this time reliable cloud information has been sparse.
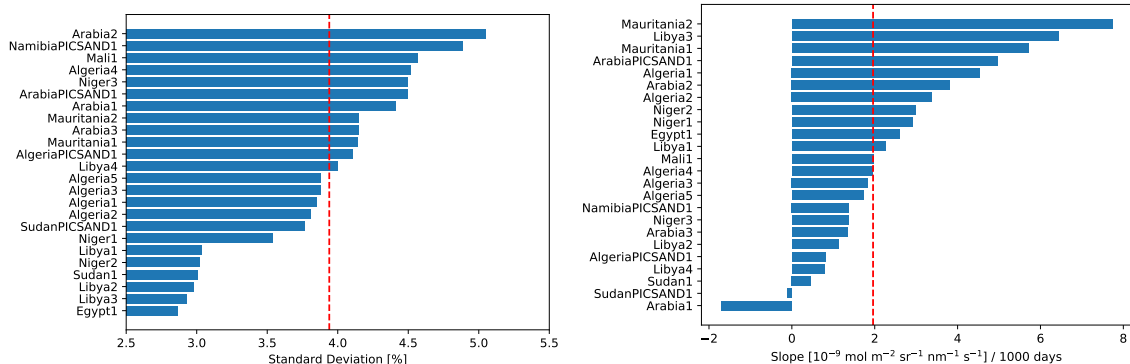
Figure 4. Sorted bar diagrams for the standard deviation of the radiance distribution of each site (left) and the slope of a linear fit, expressed in the slope per 1000 days (right). In red we show the median standard deviation and median slope for the distribution.

Interestingly, the standard deviation found for most sites is a) much larger than the uncertainty per measurement (which is estimated to be less then 0.1% Kleipool et al. (2018); van Kempen et al. (2019); Ludewig et al. (2020)), b) relatively constant for all sites in both time and magnitude. A spread of 8 to 11×10^{-9} mol m^{-2} sr^{-1} nm^{-1} s^{-1}, equivalent to 3-5% is found for all sites.

160   The results of van Kempen et al. (2019) show that instrumental variation in measurement to measurement due to detector noise is much smaller, and that the uncertainty from instrumental effects is dominated by photon noise only, which is estimated to be on the order of 0.1%). The higher measurement to measurement variation reported in Ludewig et al. (2020) seen in the irradiance were attributed to electronic noise. However, due to more in-depth analysis carried out, it is now attributed to surface roughness of the diffusers (van Kempen & Ludewig, priv. comm). The distribution of viewing angles from TROPOMI SWIR
165   over a full year is large, due to the large swath of TROPOMI that allows for daily global coverage.

From investigations of the TROPOMI-SWIR data above the RailRoad Valley site compared to on-ground measurements, we attribute the derived standard deviation to non-Lambertian reflections of the sandy surface (van Kempen et al., in prep).

Individual site heterogeneity is considered to be a small effect. Site heterogeneity would effect the results due to the varying size of the TROPOMI pixel, and exhibit itself as a pattern repeated every 16 days, equivalent to the orbital cycle of S-5p. This
170   pattern varies by site and depends on the more precise BRDF proporties of the surfaces. No clear evidence for patterns on these timescales can be seen or derived from Figure 2. Heterogeneity would also be detectable as a correlation between the values SHOM of 20 km or 100 km of Table 2 of Bacour et al. (2019) and the derived standard deviation values of Table 3. Figure 5 shows the lack of correlation between the given site homogeneity at scales of 20 km and the standard deviation of the time series given in Table 3.

175   Linear fits found are very shallow, with typical number between 0 and 5×10^{-9} mol m^{-2} sr^{-1} nm^{-1} s^{-1} per 1,000 days. This equates to a maximum increase in transmission of 0.7% per year. The average of the slope is equal to 0.3 % per year. Note
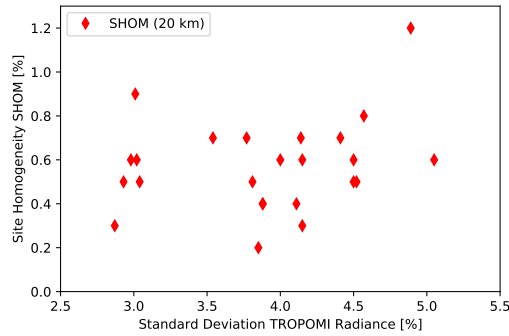
Figure 5. Comparison of the relative standard deviation of the time series of radiance with the site homogeneity at 20 km (SHOM) given in Bacour et al. (2019), revealing a lack of correlation.
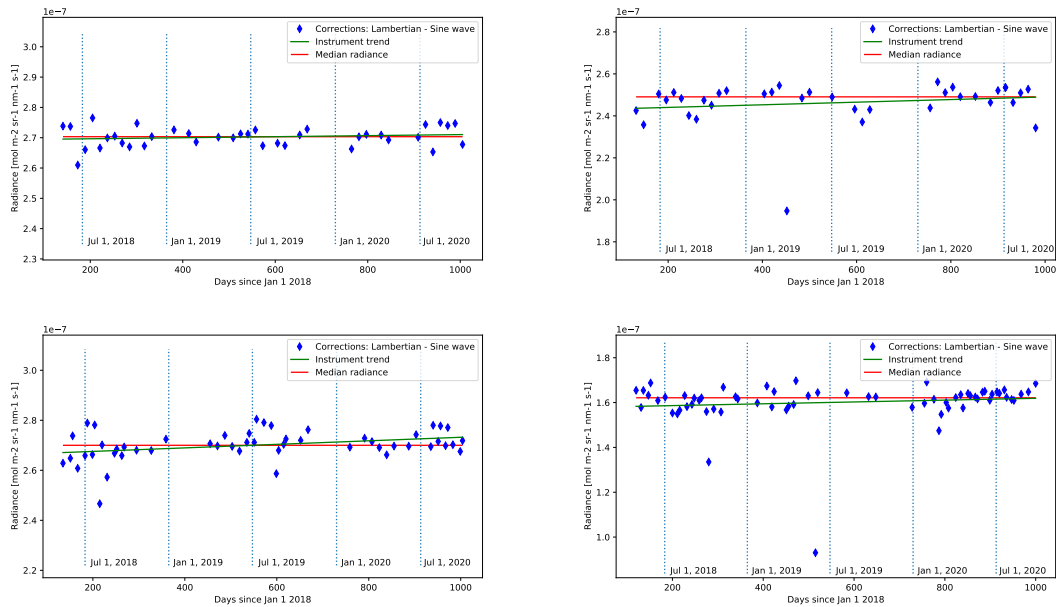
Figure 6. Continuum radiance of Egypt1 (top left), Algeria3 (top right), Libya3 (bottom left) and NamibiaPICSAND1 (bottom right) using a zenith angle filter of 7.5 degrees. Shown are all soundings over a period of more than 1,000 days, starting 28th of April 2018. The median radiance (red) and a linear fit (green) are shown with lines. Data has been corrected for the solar zenith angle at each individual overpass and assuming the surface is Lambertian. A yearly variation has been corrected using a fitted sine wave with a period of 365 days. Other sites are given in supplementary material.

that many sites are found at lower values, and a few even showing a negative slope. Given the typical standard deviation, we attribute the slopes to statistical variations. The impact on SWIR instrument degradation is discussed below.

Table 3. Median radiance, standard deviation (both absolute and relative) and slope of a linear fit for the full sample.

Site	Median Radiance $[10^{-7}]$ mol m^{-2} sr^{-1} nm^{-1} s^{-1}	St. Dev $[10^{-9}]$	%	Slope $[10^{-9}]$ mol m^{-2} sr^{-1} nm^{-1} s^{-1} per 1000 days
Algeria1	2.44	9.4	3.85	4.54
Algeria2	2.51	9.6	3.81	3.38
Algeria3	2.51	9.7	3.88	1.84
Algeria4	2.57	11.6	4.52	1.95
Algeria5	2.56	9.9	3.88	1.73
AlgeriaPICSAND1	2.54	10.4	4.11	0.82
Arabia1	2.38	10.5	4.41	-1.71
Arabia2	2.31	11.7	5.05	3.82
Arabia3	2.41	10.0	4.15	1.35
ArabiaPICSAND1	2.45	11.0	4.50	4.96
Egypt1	2.72	7.9	2.87	2.59
Libya1	2.76	8.4	3.04	2.26
Libya2	2.74	8.2	2.98	1.12
Libya3	2.71	8.0	2.93	6.44
Libya4	2.65	10.6	4.00	0.78
Mali1	2.55	11.6	4.57	1.97
Mauritania1	2.63	10.8	4.14	5.71
Mauritania2	2.63	10.9	4.15	7.73
NamibiaPICSAND1	1.63	8.0	4.89	1.38
Niger1	2.75	9.7	3.54	2.91
Niger2	2.49	7.5	3.02	2.99
Niger3	2.36	10.6	4.50	1.36
Sudan1	2.59	7.8	3.01	0.46
SudanPICSAND1	2.66	10.1	3.77	-0.10

4.1 Nadir view

180 Given the influence of non-lambertian reflection on the standard deviation, the stability of the four sites with various quality (Egypt1, Algeria3, Libya3 and NamibiaPICSAND1, see Fig. 6) is shown using only viewing angles less than 7.5 degrees from nadir. The results are given in Table 4 with the full results given for completeness. Differences are marginal, with the largest differences seen in the linear fit. For some, the standard deviation improved. The main difference was found in the reliability of the removal of the yearly variation through the 365-period sine wave. Interestingly, the fit parameters were nearly

Table 4. Median radiance, standard deviation (both absolute and relative) for the sample with a Instrument Zenith Angle (IZA) filter of 7.5 degrees.

Site	IZA 7.5 degrees		
	Median Radiance	St. Dev	
	10^{-7}	10^{-9}	%
	mol m^{-2} sr^{-1} nm^{-1} s^{-1}		
Algeria1	2.44	8.1	3.3
Algeria2	2.51	7.4	3.0
Algeria3	2.49	10.2	4.2
Algeria4	2.58	6.3	2.4
Algeria5	2.56	6.2	2.4
AlgeriaPICSAND1	2.52	10.0	4.0
Arabia1	2.39	7.2	3.0
Arabia2	2.30	7.7	3.3
Arabia3	2.42	6.5	2.7
ArabiaPICSAND1	2.45	8.3	3.4
Egypt1	2.70	3.2	1.2
Libya1	2.75	7.2	2.6
Libya2	2.76	6.2	2.2
Libya3	2.70	5.9	2.2
Libya4	2.63	8.7	3.3
Mali1	2.50	11.0	4.4
Mauritania1	2.63	12.4	4.8
Mauritania2	2.53	12.3	4.9
NamibiaPICSAND1	1.62	9.9	6.2
Niger1	2.72	12.2	4.5
Niger2	2.48	5.02	2.0
Niger3	2.36	15.0	6.5
Sudan1	2.59	7.3	2.8
SudanPICSAND1	2.69	6.4	2.4

185 identical as that derived above, with only the reliability of this fit found to be significantly worse. This is easily explained due to the significantly lower amount of data used as input for the fit. This also corroborates the conclusions on the influence of heterogeneity. Any effects if site heterogeneity would be nearly eliminated as the pixels are nearly identical in size and viewing the same area. This would result in a severely reduced standard deviation, which is not observed in Table 4.

Table 5. Amplitude and period offset of fitted and subtracted sine waves.

Site	Amplitude 10^{-9} [mol m^{-2} sr^{-1} nm^{-1} s^{-1}]	Offset Days
Algeria1	6.86	-14.9
Algeria2	7.12	-15.5
Algeria3	4.99	2.4
Algeria4	4.03	24.9
Algeria5	4.70	18.6
AlgeriaPICSAND1	6.43	0.3
Arabia1	1.71	203.5
Arabia2	0.98	35.4
Arabia3	4.61	84.3
ArabiaPICSAND1	4.67	79.6
Egypt1	4.51	44.6
Libya1	3.94	-7.3
Libya2	4.96	-8.8
Libya3	3.58	-12.9
Libya4	5.99	32.2
Mali1	11.57	-41.4
Mauritania1	11.35	-40.5
Mauritania2	9.95	-42.0
NamibiaPICSAND1	3.14	133.8
Niger1	6.03	-29.1
Niger2	4.21	-22.7
Niger3	4.47	-29.0
Sudan1	5.21	1.38
SudanPICSAND1	7.85	-16.6

4.2 Origin of yearly variation

190 The sine wave used to correct an observed yearly variation is attributed to the BRDF effect It is not instrumental in nature given the results of van Kempen et al. (2019) and ongoing monitoring (see www.sron.nl/tropomi-swir-monitoring/) and should thus be attributed to a feature present in the surface. The amplitudes and period offsets with respect to January 1st 2018 are given in Table 5. Example fits are given in the appendix. It appears that variation in this yearly variation is regionally distributed. Sites in the south-western variation (Mauritania, Mali, Niger and Algeria1 and Algeria2, have a larger amplitude (6 to 11) period

195 offset with a small negative offset in days w.r.t. to the reference day of Jan 1 2018 while eastern Sahara sites (Libya, Egypt,

Sudan) tend to have smaller amplitudes (4-5) and show a slight positive offset. The Namibian desert site is clearly different due to its location on the southern hemisphere. The sites in the Arabian desert are grouped south (Arabia1 and Arabia2) and north (Arabia3 and ArabiaPICSAND1) in amplitude, but show no correlation in period. Arabia1 has a relatively large offset.

As to the origin, four possibilities are entertained. Several others are either disqualified or limited to relaively small contributions. The first is shadowing of dune formation, caused by site heterogeneity. Bacour et al. (2019) investigated site homogeneity for both the original positions of Cosnefroy et al. (1996) and their own more optimal locations. The latter, used here, are significantly more homogeneous at scales of both 20 and 100 km. Given the typical pixel size of TROPOMI, homogeneity at 20 km is relevant . Differences are seen in Google maps (Bacour et al., 2019), but in general the sites are homogeneous down to a few percent or less. If dune formation would be a large factor, minima would be expected around mid-December due to the solar zenith angle. This minimum corresponds to an offset in days equal to approximately 80. In addition, the sole southern hemisphere location would show a minimum during late June and an offset of 260 days. This offset would also not be dependent on site, while amplitude can be. Both are not seen Table 3. However, dune formation and site heterogeneity in general can be more chaotic and thus needs to be investigated further.

The second possibiliy is a dependency to rock or sand composition for reflectance and BRDF, another component in site heterogeneity. Our data is insufficient to make any conclusions on this. However, it would be related to location and size of hotspot and would be incompatible with the observation that the yearly variation is detected with similar amplitudes using only nadir overpasses. This hypothesis does warrant deeper investigation.

Third, given the ISRF width (van Hees et al., 2018) some wings of absorption features are within the range. Such line absorption could show a yearly variation.These absorptions are very small ($<0.5\%$) and are not part of either CH_4 or H_2O absorption features. Identifying any line contamination beyond CH_4 and H_2O is considered beyond the scope of this paper. Given the expected magnitude, this possibility is considered to be only a very remote possibility.

Last but not least, the lack of atmospheric correction likely influences the results. At SWIR continuum wavelengths this correction is dominated by varying quantities of aerosol in the atmosphere as a function of atmosphere height. This effect likely can contribute to yearly variations, but due to the opacity of aerosols at these wavelengths (0.05 or less) is expected to be smaller than the BRDF effects.

Several possibilities are ruled out. First, any instrument stability that would be yearly in scope would be detectable either with the on-board calibration and/or reflectance average that is also monitored (van Kempen et al., 2019; Ludewig et al., 2020). These show limits less than 0.3%, in line with the results of the linear fits. Another possibility is the varying distance between the Sun and the Earth. Although this variation is expected to be of similar magnitude ($\sim$2.25%, it would also cause two features not observed. First perihelion occurs near January 5th. Sine offsets would thus be consistely fitted at 90 or +270 days in Table 5. Deviations from this fit are not expected to be larger than 10%. However fits with a complete 180 degree phase difference are found. TROPOMI radiance is corrected for the Earth-Sun distance (See TROPOMI L1b ATBD: S5P-KNMI-L01B-0009-SD).

Although the second option (BRDF) appears to be the most likely, the other three options cannot be excluded, in particular the effect of aerosol in the atmospheric correction, nor can it be excluded all contribute to the variation and/or spreads observed. A future publication (van Kempen et al., in prep) will investigate the BRDF and the effect of the atmospheric corrections

including aerosols, including this yearly variation. It will do so over a single instrumented site (RailRoad Valley) to provide validation against ground measurements.

5 Conclusions

The results above show that the sample of Saharan PICS are well-suited as a validation of the instrument stability, both using
235   viewing angles up to 50 degrees and to only 7.5 degrees. The standard deviations seen are similar from site to site. This was achieved by a strict filter on clouds (cloud coverage of <0.02) and correcting for the solar zenith angle during any overpass. In addition, observed yearly variations were removed by fitting a sine wave with a period of a single year. The results clearly show no evidence for TROPOMI-SWIR instrument degradation or increased transmission. The results validate the conclusions shown in van Kempen et al. (2019) with a limit of 0.5% over the first 1,000 days. Note that the internal calibration suite shows
240   no degradation or increased transmission down to levels of $\sim$0.1% over the first year. Subsequent monitoring[7] has revealed this to hold over the first 1,000 days as well.

The lack of difference using filters with both 50 and 7.5 degrees is somewhat surprising given the attributed influence of non-lambertian reflectances (which peak at angles of 20-30 degrees from zenith) and the inclusion of larger TROPOMI pixels (due to the swath size of TROPOMI). Note however that following Bacour et al. (2019) most sites were assumed to be spatially
245   homogeneous. This likely explains the lack of influence of larger pixels at larger viewing angles. Subsequently, we can conclude that the spatial homogeneity conclusions indeed apply to SWIR wavelengths following this study.

The variation from site to site is also relatively small, but do appear to be correlated by region. The Namibian desert has a significantly lower radiance, while the sites in the Arabian desert only show a lower radiance by about 3-5% as compared to the Saharan Desert. Differences within the Sahara (i.e. east-west or per country) appear to be marginal and warrant further
250   investigation.

The most obvious improvements that can be made are in the field of non-lambertian effects. TROPOMI covers a very large range of angles. Given the recent conclusions of the BRDF studies in e.g. RailRoad Valley (Bruegge et al., 2019a), measurements at larger viewing angles must be corrected to make comparisons.

In conclusions, future SWIR spectrometers should, if possible, prefer the usage of internal calibration sources or solar cali-
255   bration over the usage of PICS as the primary means for instrument calibration. However, for so-called small-sat applications with total weight and/or life-limited instrument constraints, these results show that monitoring of suitable PICS offer a suitable, albeit a relatively more inaccurate, alternative.

Code and data availability. All L1b-data is freely available through the Copernicus Open Access hub (https://scihub.copernicus.eu). The pys5p code that is the basis of the analysis code can be found on Zenodo (https://zenodo.org/record/4073256) under DOI 10.5281/zen-
260   odo.4073256 intermediate results are available through SRON.

---

[7]See www.sron.nl/tropomi-swir-monitoring/

Competing interests. There are no known competing interests.

Author contributions. The work was started by FO under supervision of TvK as part of an internship. TvK expanded conclusions and additional work, including writing the paper. The base software packages were written and provided by RvH.

Acknowledgements. We thank the team that has realized the TROPOMI instrument, consisting of the partnership between Airbus Defence and Space Netherlands, Royal Netherlands Meteorological Institute (KNMI), SRON Netherlands Institute for Space Research (TNO), and Netherlands Organisation for Applied Scientific Research (TNO), Netherlands Space Office (NSO), and European Space Agency. This research contains modified Copernicus Sentinel data of 2018, 2019 and 2020. The work of TvK is funded by the TROPOMI national program from the NSO. We would like to acknowledge the fruitful discussions with several members of the Earth Science Group at SRON (Ilse Aben, Paul Tol, Tobias Borsdorff, Jochen Landgraf and Alba Llorente).

References

Bacour, C., Briottet, X., Bréon, F.-M., Viallefont-Robinet, F., and Bouvet, M.: Revisiting Pseudo Invariant Calibration Sites (PICS) Over Sand Deserts for Vicarious Calibration of Optical Imagers at 20 km and 100 km Scales, Remote Sensing, 11, 1166, https://doi.org/10.3390/rs11101166, 2019.

Borsdorff, T., aan de Brugh, J., Hu, H., Hasekamp, O., Sussmann, R., Rettinger, M., Hase, F., Gross, J., Schneider, M., Garcia, O., Stremme, W., Grutter, M., Feist, D. G., Arnold, S. G., De Mazière, M., Sha, M. K., Pollard, D. F., Kiel, M., Roehl, C., Wennberg, P. O., Toon, G. C., and Landgraf, J.: Mapping carbon monoxide pollution from space down to city scales with daily global coverage, Atmospheric Measurement Techniques, 11, 5507–5518, https://doi.org/10.5194/amt-11-5507-2018, 2018.

Bouvet, Thome, Berthelot, Bialek, Czapla-Myers, Fox, Goryl, Henry, Ma, Marcq, Meygret, Wenny, and Woolliams: RadCalNet: A Radiometric Calibration Network for Earth Observing Imagers Operating in the Visible to Shortwave Infrared Spectral Range, Remote Sensing, 11, 2401, https://doi.org/10.3390/rs11202401, 2019.

Bruegge, Coburn, Elmes, Helmlinger, Kataoka, Kuester, Kuze, Ochoa, Schaaf, Shiomi, and Schwand ner: Bi-Directional Reflectance Factor Determination of the Railroad Valley Playa, Remote Sensing, 11, 2601, https://doi.org/10.3390/rs11222601, 2019a.

Bruegge, C. J., Crisp, D., Helmlinger, M. C., Kataoka, F., Kuze, A., Lee, R. A., McDuffie, J. L., Rosenberg, R. A., Schwand ner, F. M., Shiomi, K., and Yu, S.: Vicarious Calibration of Orbiting Carbon Observatory-2, IEEE Transactions on Geoscience and Remote Sensing, 57, 5135–5145, https://doi.org/10.1109/TGRS.2019.2897068, 2019b.

Chander, G., Hewison, T. J., Fox, N., Wu, X., Xiong, X., and Blackwell, W. J.: Overview of Intercalibration of Satellite Instruments, IEEE Transactions on Geoscience and Remote Sensing, 51, 1056–1080, https://doi.org/10.1109/TGRS.2012.2228654, 2013.

Cosnefroy, H., Leroy, M., and Briottet, X.: Selection and characterization of Saharan and Arabian desert sites for the calibration of optical satellite sensors, Remote Sensing of Environment, 58, 101–114, https://doi.org/10.1016/0034-4257(95)00211-1, 1996.

Hu, H., Landgraf, J., Detmers, R., Borsdorff, T., Aan de Brugh, J., Aben, I., Butz, A., and Hasekamp, O.: Toward Global Mapping of Methane With TROPOMI: First Results and Intersatellite Comparison to GOSAT, Geophysical Research Letters, 45, 3682–3689, https://doi.org/10.1002/2018GL077259, 2018.

Kataoka, F., Crisp, D., Taylor, T., O'Dell, C., Kuze, A., Shiomi, K., Suto, H., Bruegge, C., Schwandner, F., Rosenberg, R., Chapsky, L., and Lee, R.: The Cross-Calibration of Spectral Radiances and Cross-Validation of CO2 Estimates from GOSAT and OCO-2, Remote Sensing, 9, 1158, https://doi.org/10.3390/rs9111158, 2017.

Kleipool, Q., Ludewig, A., Babic, L., Bartstra, R., Braak, R., Dierssen, W., Dewitte, P.-J., Kenter, P., Landzaat, R., Leloux, J., Loots, E., Meijering, P., van der Plas, E., Rozemeijer, N., Schepers, D., Schiavini, D., Smeets, J., Vacanti, G., Vonk, F., and Veefkind, P.: Prelaunch calibration results of the TROPOMI payload on-board the Sentinel 5 Precursor satellite, Atmospheric Measurement Techniques Discussions, 2018, 1–67, https://doi.org/10.5194/amt-2018-25, https://www.atmos-meas-tech-discuss.net/amt-2018-25/, 2018.

Kuze, A., Taylor, T. E., Kataoka, F., Bruegge, C. J., Crisp, D., Harada, M., Helmlinger, M., Inoue, M., Kawakami, S., Kikuchi, N., Mitomi, Y., Murooka, J., Naitoh, M., O'Brien, D. M., O'Dell, C. W., Ohyama, H., Pollock, H., Schwandner, F. M., Shiomi, K., Suto, H., Takeda, T., Tanaka, T., Urabe, T., Yokota, T., and Yoshida, Y.: Long-Term Vicarious Calibration of GOSAT Short-Wave Sensors: Techniques for Error Reduction and New Estimates of Radiometric Degradation Factors, IEEE Transactions on Geoscience and Remote Sensing, 52, 3991–4004, https://doi.org/10.1109/TGRS.2013.2278696, 2014.

305 Lacherade, S., Fougnie, B., Henry, P., and Gamet, P.: Cross Calibration Over Desert Sites: Description, Methodology, and Operational Implementation, IEEE Transactions on Geoscience and Remote Sensing, 51, 1098–1113, https://doi.org/10.1109/TGRS.2012.2227061, 2013.

Ludewig, A., Kleipool, Q., Bartstra, R., Land zaat, R., Leloux, J., Loots, E., Meijering, P., van der Plas, E., Rozemeijer, N., Vonk, F., and Veefkind, P.: In-flight calibration results of the TROPOMI payload on board the Sentinel-5 Precursor satellite, Atmospheric Measurement
310 Techniques, 13, 3561–3580, https://doi.org/10.5194/amt-13-3561-2020, 2020.

Pandey, S., Gautam, R., Houweling, S., Denier van der Gon, H., Sadavarte, P., Borsdorff, T., Hasekamp, O., Landgraf, J., Tol, P., van Kempen, T., Hoogeveen, R., van Hees, R., Hamburg, S. P., Maasakkers, J. D., and Aben, I.: Satellite observations reveal extreme methane leakage from a natural gas well blowout, Proceedings of the National Academy of Science, 116, 26 376–26 381, https://doi.org/10.1073/pnas.1908712116, 2019.

315 Rahman, H., Pinty, B., and Verstraete, M. M.: Coupled surface atmosphere reflectance (CSAR) model: 2. Semiempirical surface model usable with NOAA advanced very high resolution radiometer data, Journal of Geophysical Research, 98, 20,791–20,801, https://doi.org/10.1029/93JD02072, 1993a.

Rahman, H., Verstraete, M. M., and Pinty, B.: Coupled surface-atmosphere reflectance (CSAR) model: 1. Model description and inversion on synthetic data, Journal of Geophysical Research, 98, 20,779–20,789, https://doi.org/10.1029/93JD02071, 1993b.

320 Schaaf, C. B., Liu, J., Gao, F., and Strahler, A. H.: Aqua and Terra MODIS Albedo and Reflectance Anisotropy Products, vol. 11, p. 549, https://doi.org/10.1007/978-1-4419-6749-7_24, 2011.

Tol, P. J. J., van Kempen, T. A., van Hees, R. M., Krijger, M., Cadot, S., Snel, R., Persijn, S. T., Aben, I., and Hoogeveen, R. W. M.: Characterization and correction of stray light in TROPOMI-SWIR, Atmospheric Measurement Techniques, 11, 4493–4507, https://doi.org/10.5194/amt-11-4493-2018, https://www.atmos-meas-tech.net/11/4493/2018/, 2018.

325 van Hees, R. M., Tol, P. J. J., Cadot, S., Krijger, M., Persijn, S. T., van Kempen, T. A., Snel, R., Aben, I., and Hoogeveen: Determination of the TROPOMI-SWIR instrument spectral response function, Atmospheric Measurement Techniques, 11, 3917–3933, https://doi.org/10.5194/amt-11-3917-2018, https://www.atmos-meas-tech.net/11/3917/2018/, 2018.

van Kempen, T. A., van Hees, R. M., Tol, P. J. J., Aben, I., and Hoogeveen, R. W. M.: In-flight calibration and monitoring of the Tropospheric Monitoring Instrument (TROPOMI) short-wave infrared (SWIR) module, Atmospheric Measurement Techniques, 12, 6827–6844,
330 https://doi.org/10.5194/amt-12-6827-2019, 2019.

Veefkind, J. P., Aben, I., McMullan, K., Förster, H., de Vries, J., Otter, G., Claas, J., Eskes, H. J., de Haan, J. F., Kleipool, Q., van Weele, M., Hasekamp, O., Hoogeveen, R., Landgraf, J., Snel, R., Tol, P., Ingmann, P., Voors, R., Kruizinga, B., Vink, R., Visser, H., and Levelt, P. F.: TROPOMI on the ESA Sentinel-5 Precursor: A GMES mission for global observations of the atmospheric composition for climate, air quality and ozone layer applications, rse, 120, 70–83, https://doi.org/10.1016/j.rse.2011.09.027, 2012.

335 Zhang, Y., Gautam, R., Pandey, S., Omara, M., Maasakkers, J. D., Sadavarte, P., Lyon, D., Nesser, H., Sulprizio, M. P., Varon, D. J., Zhang, R., Houweling, S., Zavala-Araiza, D., Alvarez, R. A., Lorente, A., Hamburg, S. P., Aben, I., and Jacob, D. J.: Quantifying methane emissions from the largest oil-producing basin in the United States from space, Science Advances, 6, https://doi.org/10.1126/sciadv.aaz5120, https://advances.sciencemag.org/content/6/17/eaaz5120, 2020.